Dalton Transactions

ROYAL SOCIETY OF CHEMISTRY

PAPER

View Article Online
View Journal | View Issue

Cite this: *Dalton Trans.*, 2025, **54**, 5685

Cu- and P-co-doped nitrogen-doped hierarchical carbon for enhanced oxygen reduction reaction in zinc–air batteries†

Zhongyuan Rong,[a] Mengwei Li,[a] Yijie Deng *[a] and Haibo Tang*[b]

Received 11th November 2024,
Accepted 17th February 2025

DOI: 10.1039/d4dt03156c

rsc.li/dalton

High-performance Fe-based nitrogen-doped carbon oxygen reduction catalysts have been widely reported, but the Fenton reaction faced by such catalysts has hindered their practical application in fuel cells. The development of inexpensive, effective, and durable non-Fe nitrogen-doped carbon electrocatalysts is important for advancing fuel cell technology. In this work, we have introduced a molecular coordination chemistry method to synthesize a Cu- and P-co-doped nitrogen-doped hierarchical carbon (Cu–P–N–C) oxygen reduction reaction (ORR) electrocatalyst by pyrolyzing a mixture of phytate and melamine. The refined Cu–P–N–C material showcased a three-dimensional, porous, interconnected nanosheet structure with an ultra-high specific surface area and an abundance of active sites. The Cu–P–N–C catalyst displayed a half-wave potential ($E_{1/2}$) of 0.86 V_{RHE}, higher than that of commercial Pt/C in 0.1 M KOH. It was also found to maintain an impressive long-term stability, retaining 95.4% of its initial activity after extensive testing. When integrated into zinc–air batteries (ZABs), the Cu–P–N–C electrocatalyst was observed to deliver exceptional performance, achieving a high peak power density of 164.5 mW cm^{-2}, a promising specific capacity of 807 mA h g^{-1}, and remarkable stability. These findings underscore the potential of Cu–P–N–C as a potential candidate for next-generation ORR electrocatalysts in new energy devices.

1. Introduction

In recent years, the urgent need to achieve enhanced energy efficiency and environmental sustainability has led to the development of many renewable energy technologies, including supercapacitors,[1,2] fuel cells,[3,4] sodium-ion batteries,[5,6] Li-ion batteries and metal–air batteries.[7–9] As a typical class of metal–air batteries, zinc–air batteries (ZABs) have emerged as a promising option due to their low cost, minimal environmental impact, high energy density, and renewability. However, the sluggish four-electron oxygen reduction reaction (ORR) kinetic process at the cathode of a ZAB makes obtaining high electrochemical reaction rates an enormous challenge.[10–12] Platinum (Pt) is the go-to material for catalyzing the ORR with superior catalytic properties. However, its current problems (high cost, insufficient stability, vulnerability to poisoning, *etc.*) have brought substantial challenges for the popularity of ORR-based energy storage devices.[13,14] To reduce reliance on precious metals, it is necessary to develop a non-precious-metal ORR catalyst that is cost-effective, highly active, and stable.

In the past years, non-precious-metal electrocatalysts have been investigated in large quantities, and have included transition metal oxides,[15,16] metal sulfides and their analogs,[17,18] and carbon-based ORR catalysts.[19–21] Doped carbon-based materials have garnered significant attention for the ORR due to their enhanced conductivity and durability. In addition to single-element doping (*e.g.*, B, N, P, S, F), multi-element doping (*e.g.*, N/P, N/F, N/S) has also been conducted, and has been reported to yield a synergic catalytic effect, which is attributed to the increased exposure of active sites and accelerated electron transfer.[22–24] Furthermore, the catalytic activity of oxygen reduction was shown to be significantly increased by doping a transition metal (*e.g.*, Fe, Co). High-performance Fe-doped N-doped carbon oxygen reduction catalysts have been widely studied, but the Fenton reaction from Fe-based catalysts would destroy the structure of the proton-exchange membrane, leading to reduced stability. Developing high-activity non-Fe nitrogen-doped carbon electrocatalysts is essential for advancing fuel cell energy technologies.

[a]*School of Resource Environment and Safety Engineering, University of South China, Hengyang 421001, China. E-mail: dengyijie19891009@163.com*
[b]*National energy key laboratory for new hydrogen-ammonia energy technologies, Foshan Xianhu Laboratory, Foshan 528200, China. E-mail: tanghaibo@xhlab.cn*
†Electronic supplementary information (ESI) available: Experiments, Fig. S1–Fig. S12, and Tables S1, S2. See DOI: https://doi.org/10.1039/d4dt03156c

For metal-based ORR catalysts, as metal atoms tend to agglomerate to form large, low-activity metal particles during high-temperature pyrolysis of precursors, and as such agglomeration can significantly impair the catalyst activity and the longevity of the battery, specific processes are employed to prevent the metal atoms from forming large-scale, low-activity metal particles during preparation. In this study, we have developed a co-coordination approach that significantly suppresses the formation of large, less reactive phosphate nanoparticles. The resulting material, denoted as Cu–P–N–C, is characterized by an abundance of Cu–N and P–N active sites and a unique architecture that enhances its catalytic performance. Notably, under alkaline conditions, Cu–P–N–C achieves a half-wave potential ($E_{1/2}$) of 0.86 V_{RHE}, which is higher than that of the commercial benchmark Pt/C catalyst. Furthermore, it demonstrates remarkable durability, with a current loss rate of less than 5% after 40 000 s of continuous operation. In zinc–air batteries, a Cu–P–N–C-based system delivers distinguished power density and specific capacity.

2. Results and discussion

The process used to manufacture the Cu–P–N–C electrocatalyst is depicted in Fig. 1. Initially, copper acetate monohydrate was dissolved in a phytic acid aqueous solution; the obtained Cu^{2+}-coordinated phytic acid sample was mixed with a zinc acetate solution, forming the Cu–PA–Zn precursor. The Cu–PA–Zn was combined with melamine, and the resulting mixture was annealed at 550 °C under argon protection. At the 550 °C, melamine transformed to graphitic carbon nitride (g-C_3N_4).[25] When the temperature was gradually increased to 950 °C, a black catalyst material was obtained. To remove unstable species, this black catalyst sample need to undergo acid leaching by sulfuric acid solution. The obtained material was subjected to a secondary carbonization step, ultimately yielding Cu–P–N–C catalyst. The g-C_3N_4 is prone to thermal decomposition at temperatures exceeding 710 °C, forming a mass of corrosive gases containing nitrogen. The etching effect of corrosive gases containing nitrogen on the carbon skeleton is helpful for promoting the formation of a porous architecture and active sites.[26] To deeply understand the advantage of the co-coordination method and the role of Cu doping, Cu–P–N–C (Cm) was prepared by pyrolyzing a physical mixture of PA–Zn and copper acetate monohydrate; furthermore, the P–N–C catalyst was synthesized without copper salt.

The morphology of the produced material was examined employing scanning electron microscopy (SEM). As shown in Fig. 2a and c, the Cu–P–N–C and Cu–P–N–C(Cm) catalysts each displayed a well-defined 3D porous structure with interconnected nanosheets. Transmission electron microscopy (TEM) was conducted to further uncover microstructural features. As shown in the Fig. 2b and d, in the TEM images of the Cu–P–N–C and Cu–P–N–C(Cm) catalysts, dispersed nanoparticles can be clearly seen. High-resolution TEM (HRTEM) images, shown in Fig. 2b and S2,† indicated that the phosphate nanoparticles being protected within graphite layers, and thus these low-activity nanoparticles cannot be completely removed. Furthermore, the nanoparticles in the Cu–P–N–C catalyst have an average diameter of approximately 20 nm, indicative of slight agglomeration and much smaller than those in the Cu–P–N–C(Cm) catalyst (~70 nm). This result suggested that the co-coordination method is conducive to reducing the formation of large, low-activity phosphate nanoparticles. Furthermore, elemental mapping (Fig. 2e–i) substantiated an expected uniform distribution of copper, phosphorus, and nitrogen elements outside the nanoparticles within the carbon matrix.

The X-ray diffraction (XRD) patterns acquired of Cu–P–N–C, Cu–P–N–C(Cm), and P–N–C (Fig. 3a) confirmed the coexistence of the composite phases of $Cu_3(PO_4)_2$ and $Zn_3(PO_4)_2$. Diffraction peaks were observed at 40°, 44.3°, 46.3°, and 47.1°, corresponding to the (200), (220), (003), and (113) crystal planes of triclinic $Cu_3(PO_4)_2$ (PDF#01-080-0991), respectively, and at 32.7°, 37.4°, 46.8°, 48.4°, 50.2°, and 56.1°, corresponding to the (211), (310), (−222), (400), (−312), and (−113) crystal planes of monoclinic $Zn_3(PO_4)_2$ (PDF#00-030-1490), respectively. In addition, the Raman spectra acquired of Cu–P–N–C, Cu–P–N–C(Cm), and P–N–C (Fig. 3b) exhibited two main peaks, at ~1350 cm^{-1} (D band) and ~1587 cm^{-1} (G band),

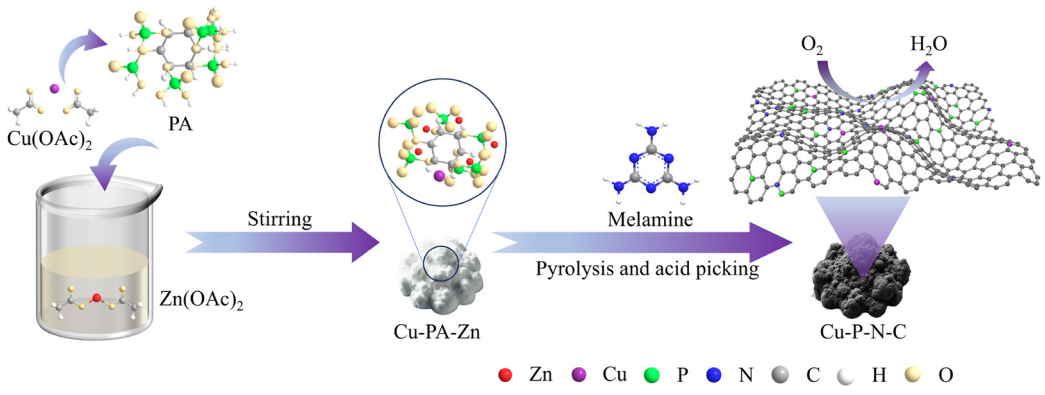

Fig. 1 Schematic of the preparation of Cu–P–N–C.

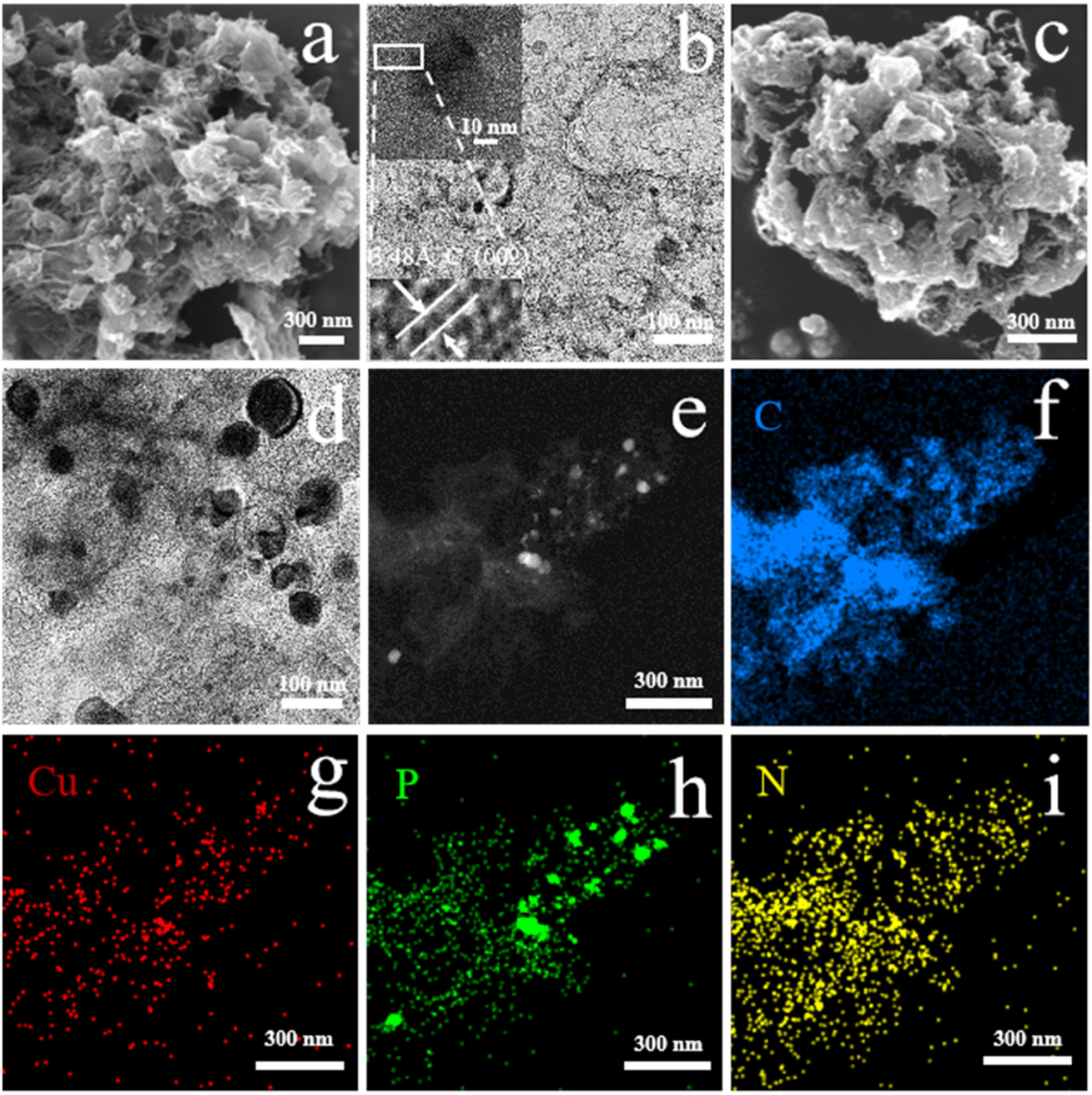

Fig. 2 (a) SEM and (b) TEM and high-resolution TEM (HRTEM) images of Cu–P–N–C. (c) SEM and (d) TEM images of Cu–P–N–C(Cm). (e–i) HAADF image and elemental mapping of Cu–P–N–C.

corresponding to defect carbon and sp^2-hybridized graphite carbon, respectively.[27] The ratio of the intensities of these peaks (I_D/I_G ratio) for Cu–P–N–C and that for Cu–P–N–C(Cm) were each higher than that for P–N–C (1.068), indicative of the doping of Cu promoting the generation of more defects, exposing more active sites. Furthermore, the I_D/I_G ratio for Cu–P–N–C was observed to be slightly lower than that for Cu–P–N–C (Cm), suggestive of the co-coordination method for doping copper leading to higher graphitization and higher electrical conductivity.

The N_2 adsorption–desorption isotherms acquired for the Cu–P–N–C, Cu–P–N–C(Cm), and P–N–C samples are depicted in Fig. 3c. These isotherms curves could be clearly assigned to type IV curves with the characteristic H_4-type hysteresis loops, which suggested the presence of a microporous and mesoporous network within the carbon framework. Moreover, the etching of nitrogen-containing gases from decomposition of melamine and removal of Zn-based species were apparently responsible for the high specific surface areas recorded for Cu–P–N–C (964 $m^2\ g^{-1}$), Cu–P–N–C(Cm) (849 $m^2\ g^{-1}$), and P–

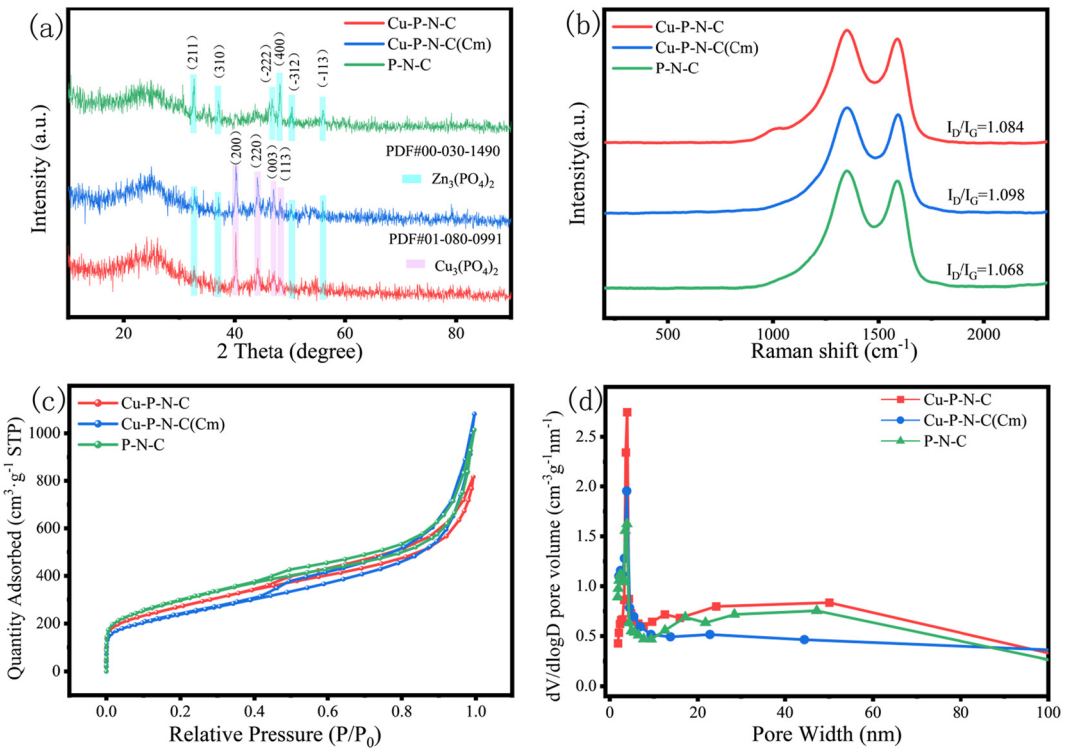

Fig. 3 (a) XRD patterns, (b) Raman spectra, (c) N_2 adsorption–desorption isotherms, and (d) pore size distributions of Cu–P–N–C, Cu–P–N–C(Cm) and P–N–C.

N–C (1065 m^2 g^{-1}), consistent with the SEM and TEM results. As displayed in Fig. 3d, the pore size distribution curves of the three samples further demonstrated a rich microporous–mesoporous architecture. From Fig. 3d, with the introduction of copper salt, the proportion of mesopores in the catalyst material increased. A balanced microporous–mesoporous structure has been deemed to be instrumental in enhancing electron and mass transport of oxygen-related species, and hence efficiently catalyzing the ORR.[28–30]

The chemical bonding environments of the catalysts were probed using X-ray photoelectron spectroscopy (XPS). The survey spectra for Cu–P–N–C, Cu–P–N–C(Cm), and P–N–C, presented in Fig. 4a, revealed the presence of Cu, P, N, C, and O elements within the Cu–P–N–C catalyst, and the quantification of atomic percentages of these elements indicated that the highest nitrogen content (4.11%) was in the Cu–P–N–C catalyst, suggestive of the incorporation of Cu enhancing the immobilization of nitrogen atoms on the carbon matrix. The signal in the N 1s region of each of the Cu–P–N–C and Cu–P–N–C(Cm) spectra can be deconvoluted into five peaks: pyridinic N (~398.3 eV), Cu–N (~399 eV), pyrrolic N (~400.2 eV), graphitic N (~401.4 eV), and oxidized N (~403.9 eV) (Fig. 4b).[31–34] As shown in Fig. 4d, our XPS analyses indicated that the Cu–P–N–C sample had the higher contents of pyridinic N and graphitic N, important since many previous investigations have indicated that pyridinic N is generally responsible for ORR activity in N-doped carbon materials and that graphitic N can enhance the conductivity of the carbon skeleton.[35,36] Moreover, our analyses indicated Cu–N bonds accounting for 17.1% of all of the bonds in Cu–P–N–C, significantly higher than their proportion in Cu–P–N–C(Cm) (11.9%), and indicated a higher proportion of Cu–P bonds in Cu–P–N–C (11.7%) than in Cu–P–N–C(Cm) (8.8%) (Fig. 4c), suggesting the co-coordination method to be more conducive to the production of Cu–N and Cu–P active sites. Furthermore, a lower oxygen content was observed for Cu–P–N–C (8.96%) than for Cu–P–N–C(Cm) (10.91%), which may be attributed to the fewer oxygen-containing phosphate species. As shown in Fig. S5,† the respective high-resolution O 1s regions of the spectra of the prepared samples each contained three binding energy peaks, corresponding to C=O, C–O, and O=C–OH.[37] The Cu–P–N–C sample clearly had a higher content of the C=O functional group; this group, due to its electron-withdrawing nature, can regulate localized charge redistribution in the carbon.[38]

The ORR catalytic performances of the samples each in a 0.1 M KOH solution were initially evaluated. The cyclic voltammetry (CV) results revealed that the Cu–P–N–C catalyst displayed the most positive and reduction peak at 0.867 V in an O_2-saturated environment, but no such signal in a N_2-saturated medium (Fig. 5a). This result confirmed that the Cu–P–N–C sample participated in the oxygen reduction reaction (ORR) process.[39,40] The linear sweep voltammetry (LSV) results (Fig. 5b) further corroborated the superior ORR catalytic performance of Cu–P–N–C, which showed a half-wave potential ($E_{1/2}$) of 0.86 V, higher than those of Cu–P–N–C(Cm) (0.848 V), P–N–C (0.851 V), and Pt/C catalyst with this result positioning

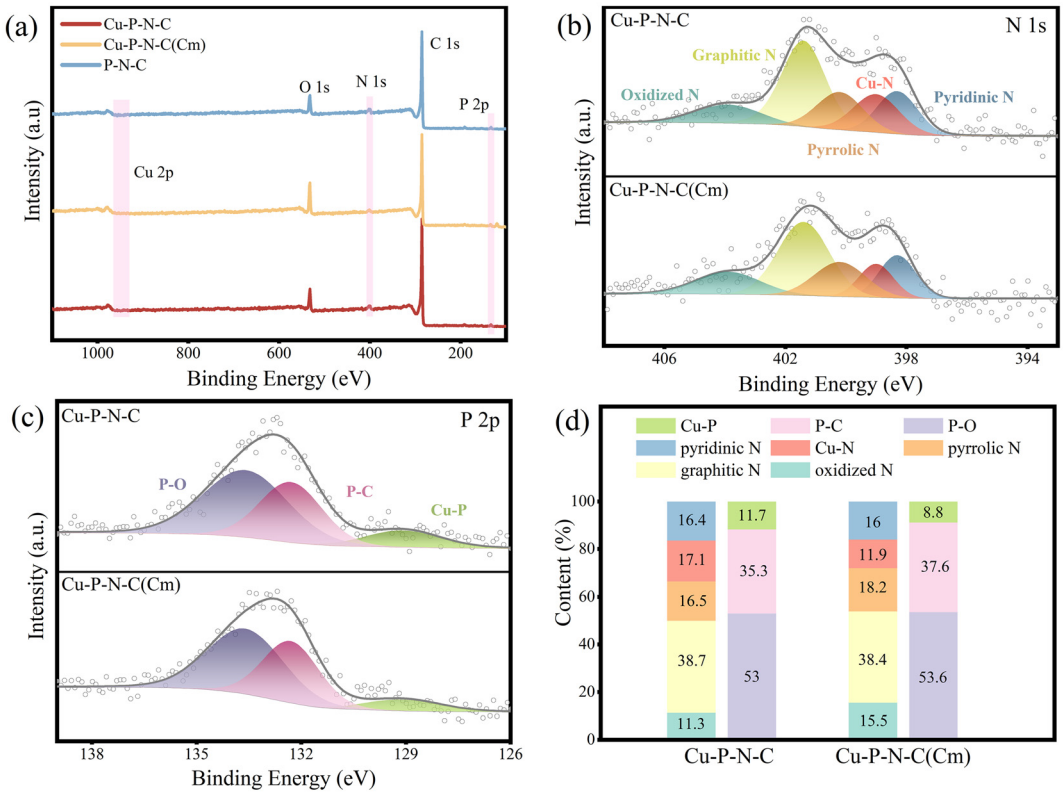

Fig. 4 (a) XPS survey spectra of Cu–P–N–C, Cu–P–N–C(Cm) and P–N–C. (b) Respective high-resolution N 1s regions of the XPS spectra of Cu–P–N–C and Cu–P–N–C(Cm). (c) Respective high-resolution P 2p regions of the XPS spectra of Cu–P–N–C and Cu–P–N–C(Cm). (d) Comparison of phosphorous and nitrogenous species in Cu–P–N–C and Cu–P–N–C-(Cm).

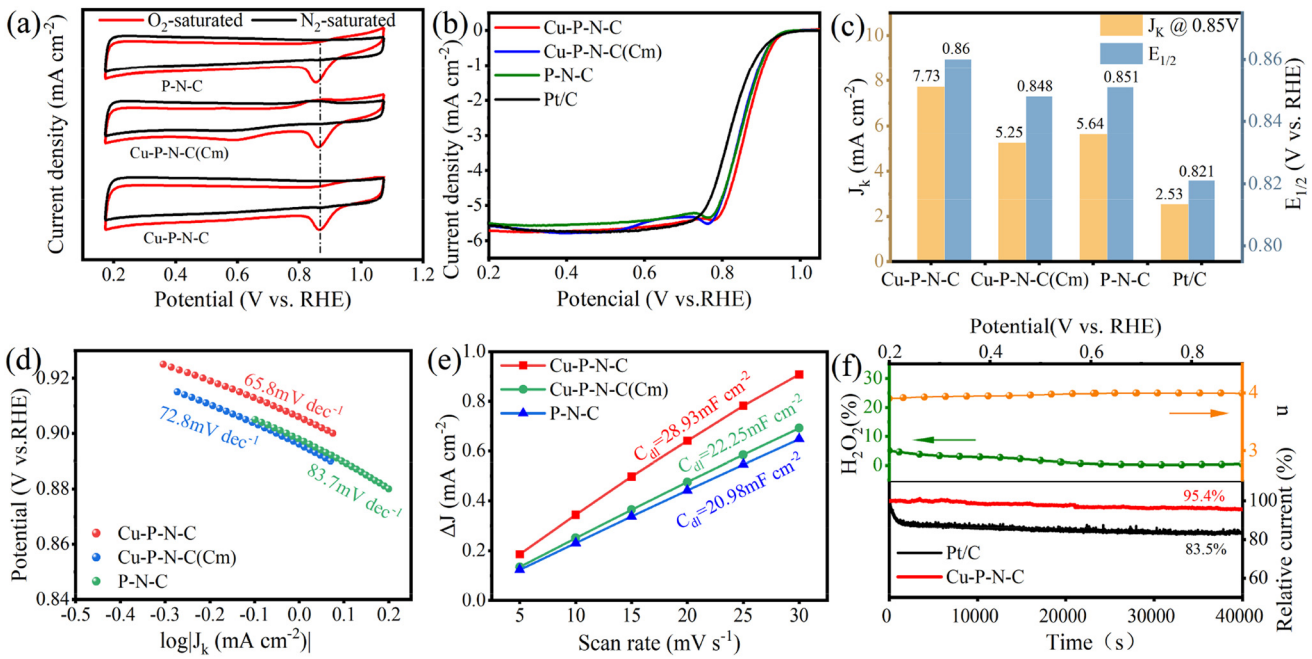

Fig. 5 The ORR performance of the studied catalysts. (a) CV curves. (b) LSV curves. (c) $E_{1/2}$ and J_k at 0.85 V *versus* RHE. (d) Tafel curves. (e) Double-layer capacitance. (f) H_2O_2 yield, electron-transfer number and long-term stability.

Cu–P–N–C among the most effective doped carbon ORR catalysts reported to date (Table S1†). Notably, despite the introduction of copper ions, the ORR performance of Cu–P–N–C (Cm) using the infiltration method was slightly poorer than that of P–N–C, attributed to the formation of large, low-activity phosphate species and a reduction in specific surface area. Furthermore, the influence of annealing temperature on the performance of the catalyst was studied. The LSV curves (Fig. S6†) pinpointed 950 °C as the optimal annealing temperature.

To gain deeper insights into the kinetic benefits of the Cu–P–N–C catalyst, an analysis of the kinetic current density (J_k) was performed. At 0.85 V, the Cu–P–N–C catalyst demonstrated a high kinetic current density, up to 7.73 mA cm^{-2}, with this value markedly superior to those of other catalysts (Fig. 5c). Furthermore, the ORR kinetic activity of the Cu–P–N–C catalyst was further studied using Tafel plots (Fig. 5d and S7†). The Tafel slope for Cu–P–N–C was determined to be 65.8 mV dec^{-1}, lower than those of other catalysts, suggesting a reduced energy barrier and more rapid kinetics for the Cu–P–N–C catalyst.[41,42]

Furthermore, electrochemical surface area (ECSA) values of the catalysts were evaluated by measuring their electrochemical double-layer capacitance (C_{dl}) levels at various scan rates. The Cu–P–N–C catalyst exhibited a notably enhanced C_{dl} value of 28.93 mF cm^{-2}, surpassing those of Cu–P–N–C(Cm) (22.25 mF cm^{-2}) and P–N–C (20.98 mF cm^{-2}) (Fig. 5e and S8†). This finding implied more active sites and a larger electrochemically active surface area presented by the Cu–P–N–C catalyst.[42] Furthermore, the ORR mechanism of these catalysts was elucidated using rotating ring-disk electrode (RRDE) technology. As shown in Fig. 5f, the Cu–P–N–C catalyst produced hydrogen peroxide with a yield below 5% and an electron transfer number (n) varying from 3.90 to 3.99 for voltages ranging from 0.2 to 0.9 V, implying high four-electron selectivity during the ORR process.[43,44] Chronoamperometry was employed to study the durability of the Cu–P–N–C catalyst. Over the course of 40 000 s of testing, the current for Cu–P–N–C slightly decreased to 95.4% of its initial value, while the commercial Pt/C sample retained only 83.5% of its initial current (Fig. 5f), which proved a favorable long-term stability of the Cu–P–N–C catalyst. The Cu–P–N–C (Cm) catalyst retained a high 95.2% of its initial current, whereas the P–N–C catalyst retained 89.1% of its initial current (Fig. S9†), indicating that the incorporation of Cu doping enhanced the long-term stability of the catalyst.

To assess the practical performance of the Cu–P–N–C catalyst in zinc–air batteries (ZABs), we constructed cathode catalysts employing the Cu–P–N–C, Cu–P–N–C(Cm), P–N–C and Pt/C, respectively (Fig. 6 and S11†). The open-circuit voltage (OCV) of the Cu–P–N–C-based ZAB was as high as 1.53 V, exceeding those of the Cu–P–N–C(Cm)-, P–N–C- and Pt/C-based ZABs (1.51 V, 1.50 V and 1.48 V) (Fig. 6b, c and S11a†). Impressively, two ZABs powered by Cu–P–N–C were capable of driving an LED display (Fig. 6d). As depicted in Fig. 6e, the Cu–P–N–C-based ZAB achieved a peak power density of 164.5 mW cm^{-2}, markedly outperforming the Pt/C-based ZAB (150.8 mW cm^{-2}). Constant current density discharge tests were performed at 20 mA cm^{-2} (Fig. 6f). The results revealed that the Cu–P–N–C catalyst exhibited a specific capacity of

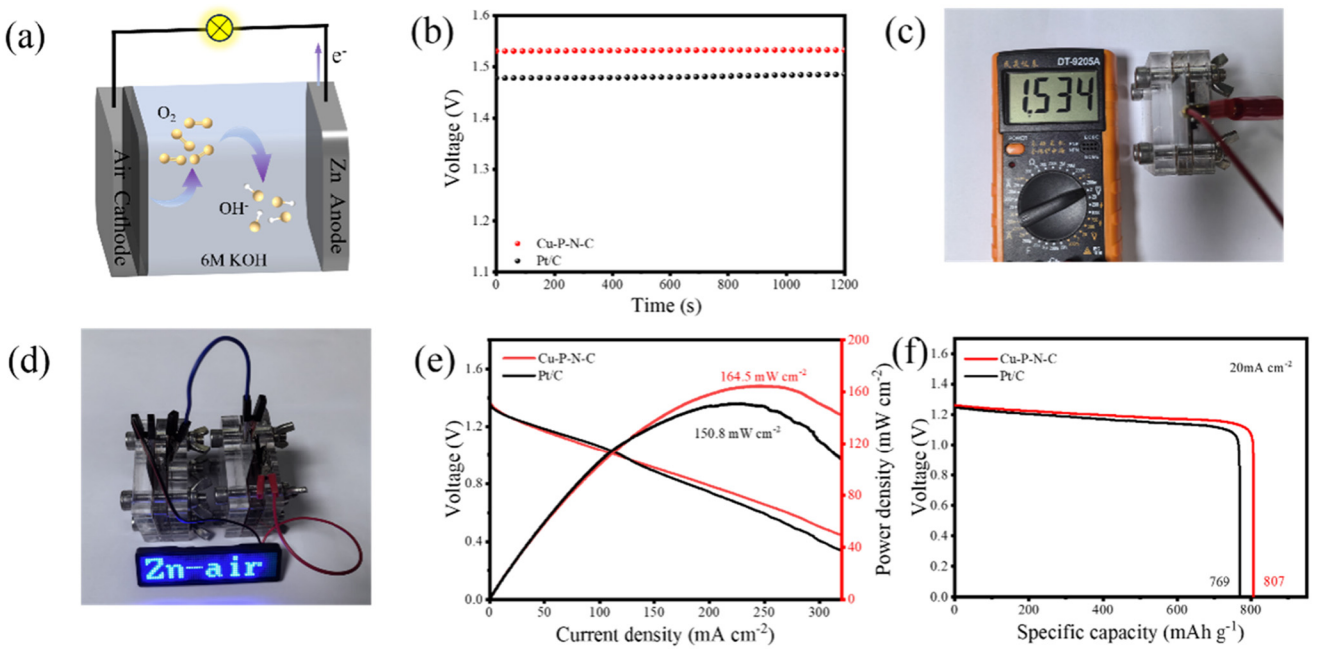

Fig. 6 (a) Diagram of the ZAB used. (b) Open-circuit voltages using the indicated ZABs. (c) Photograph showing the ZAB voltage. (d) Photograph of a LED screen lighted by Cu–P–N–C-based ZABs. (e) Polarization and power density curves for the indicated ZABs. (f) Specific discharging capacities of the indicated ZABs.

807 mA h g^{-1}, surpassing that of the Pt/C catalyst (a capacity of 769 mA h g^{-1}). To the best of our knowledge, this performance is one of the best for doped carbon catalysts tested in zinc–air battery applications (Table S2†).

3. Conclusions

A series of high-performance Cu–P–N–C catalysts was constructed by using a molecular coordination chemistry strategy, which can effectively reduce the formation of large-scale phosphate nanoparticles. Benefiting from high specific surface area (964 m^2 g^{-1}) with a microporous and mesoporous structure and the synergistic effect of the N-doped carbon layer with Cu and P, the obtained Cu–P–N–C catalyst exhibited a remarkable ORR performance and outstanding long-term stability (95.4%). And when assembled into a cathode catalyst in a ZAB, the Cu–P–N–C catalyst achieved a high power density of 164.5 mW cm^{-2}. We expect that this research will open new horizons for the development of non-Fe-derived N-doped carbon oxygen reduction catalysts for fuel cells.

Data availability

All relevant data are within the paper.

Conflicts of interest

The authors declare no competing financial interest.

Acknowledgements

This work was supported by the Guangdong Basic and Applied Basic Research Foundation (2023B1515120052, 2022A1515140048).

References

1 S. Huang, X. Zhu, S. Sarkar, *et al.*, Challenges and opportunities for supercapacitors, *APL Mater.*, 2019, **7**(10), 100901.
2 S. Zhou, Y. Zhao, K. Zhang, *et al.*, Impact-resistant supercapacitor by hydrogel-infused lattice, *Nat. Commun.*, 2024, **15**(1), 6481.
3 M. A. Abdelkareem, K. Elsaid, T. Wilberforce, *et al.*, Environmental aspects of fuel cells: A review, *Sci. Total Environ.*, 2021, **752**, 141803.
4 N. Rey-Raap, L. dos Santos-Gómez and A. Arenillas, Carbons for fuel cell energy generation, *Carbon*, 2024, 119291.
5 X. Feng, Y. Li, Y. Li, *et al.*, Unlocking the local structure of hard carbon to grasp sodium-ion diffusion behavior for advanced sodium-ion batteries, *Energy Environ. Sci.*, 2024, **17**(4), 1387–1396.
6 H. Huang, X. Wu, Y. Gao, *et al.*, Polyanionic Cathode Materials: A Comparison Between Na-Ion and K-Ion Batteries, *Adv. Energy Mater.*, 2024, **14**(14), 2304251.
7 H. Chen, H. Yuan, Z. Dai, *et al.*, Surface Gradient Ni-Rich Cathode for Li-Ion Batteries, *Adv. Mater.*, 2024, **36**(33), 2401052.
8 K. Chen, P. Barai, O. Kahvecioglu, *et al.*, Cobalt-free composite-structured cathodes with lithium-stoichiometry control for sustainable lithium-ion batteries, *Nat. Commun.*, 2024, **15**(1), 430.
9 M. Dan, X. Zhang, Y. Yang, *et al.*, Dual-axial engineering on atomically dispersed catalysts for ultrastable oxygen reduction in acidic and alkaline solutions, *Proc. Natl. Acad. Sci. U. S. A.*, 2024, **121**(6), e2318174121.
10 W. Sun, F. Wang, B. Zhang, *et al.*, A rechargeable zinc-air battery based on zinc peroxide chemistry, *Science*, 2021, **371**(6524), 46–51.
11 F. Dong, M. Wu, G. Zhang, *et al.*, Defect engineering of carbon-based electrocatalysts for rechargeable zinc-air batteries, *Chem. – Asian J.*, 2020, **15**(22), 3737–3751.
12 W. Zhang, Y. Liu, L. Zhang, *et al.*, Recent advances in isolated single-atom catalysts for zinc air batteries: A focus review, *Nanomaterials*, 2019, **9**(10), 1402.
13 Y. Nie, L. Li and Z. Wei, Recent advancements in Pt and Pt-free catalysts for oxygen reduction reaction, *Chem. Soc. Rev.*, 2015, **44**(8), 2168–2201.
14 R. Wang, J. Liu, J. Xie, *et al.*, Hollow nanocage with skeleton Ni-Fe sulfides modified by N-doped carbon quantum dots for enhancing mass transfer for oxygen electrocatalysis in zinc-air battery, *Appl. Catal., B*, 2023, **324**, 122230.
15 C. Chen, Z. J. Tang, J. Y. Li, *et al.*, MnO Enabling Highly Efficient and Stable Co–Nx/C for Oxygen Reduction Reaction in both Acidic and Alkaline Media, *Adv. Funct. Mater.*, 2023, **33**(1), 2210143.
16 Y. Yuan, J. Wang, S. Adimi, *et al.*, Zirconium nitride catalysts surpass platinum for oxygen reduction, *Nat. Mater.*, 2020, **19**(3), 282–286.
17 A. Bar-Hen, R. Bar-Ziv, T. Ohaion-Raz, *et al.*, Shelling with MoS2: Functional CuS@ MoS2 hybrids as electrocatalysts for the oxygen reduction and hydrogen evolution reactions, *Chem. Eng. J.*, 2021, **420**, 129771.
18 L. Peng, J. Wang, Y. Nie, *et al.*, Dual-ligand synergistic modulation: a satisfactory strategy for simultaneously improving the activity and stability of oxygen evolution electrocatalysts, *ACS Catal.*, 2017, **7**(12), 8184–8191.
19 Z. Chen, X. Peng, Z. Chen, *et al.*, Mass Production of Sulfur-Tuned Single-Atom Catalysts for Zn-Air Batteries, *Adv. Mater.*, 2023, **35**(15), 2209948.
20 X. T. Wu, L. J. Peng, K. Xiao, *et al.*, Rational design and synthesis of hollow Fe–N/C electrocatalysts for enhanced oxygen reduction reaction, *Chem. Commun.*, 2021, **57**(43), 5258–5261.
21 W. Li, B. Liu, D. Liu, *et al.*, Alloying Co species into ordered and interconnected macroporous carbon polyhedra for efficient oxygen reduction reaction in rechargeable zinc-air batteries, *Adv. Mater.*, 2022, **34**(17), 2109605.

22 Q. Zhai, Y. Pan and L. Dai, Carbon-based metal-free electrocatalysts: past, present, and future, *Acc. Mater. Res.*, 2021, **2**(12), 1239–1250.
23 F. Meng, S. Wang, B. Jiang, *et al.*, Coordinated regulation of phosphorus/nitrogen doping in fullerene-derived hollow carbon spheres and their synergistic effect for the oxygen reduction reaction, *Nanoscale*, 2022, **14**(29), 10389–10398.
24 M. Li, Q. Ye, S. Hou, *et al.*, Fluorine and phosphorus atoms cooperated on an N-doped 3D porous carbon network for enhanced ORR performance toward the zinc-air batteries, *J. Mater. Chem. A*, 2023, **11**(16), 8730–8738.
25 H. Zhong, L. A. Estudillo-Wong, Y. Gao, *et al.*, Cobalt-based multicomponent oxygen reduction reaction electrocatalysts generated by melamine thermal pyrolysis with high performance in an alkaline hydrogen/oxygen microfuel cell, *ACS Appl. Mater. Interfaces*, 2020, **12**(19), 21605–21615.
26 H. Yu, L. Shang, T. Bian, *et al.*, Nitrogen-Doped Porous Carbon Nanosheets Templated from g-C_3N_4 as Metal-Free Electrocatalysts for Efficient Oxygen Reduction Reaction, *Adv. Mater.*, 2016, **28**(25), 5080–5086.
27 W. Zhai, Y. He, Y. Duan, *et al.*, Densely populated trimetallic single-atoms for durable low-temperature flexible zinc-air batteries, *Appl. Catal., B*, 2024, **342**, 123438.
28 X. Lei, Q. Tang, Y. Zheng, *et al.*, High-entropy single-atom activated carbon catalysts for sustainable oxygen electrocatalysis, *Nat. Sustain.*, 2023, **6**(7), 816–826.
29 S. H. Lee, J. Kim, D. Y. Chung, *et al.*, Design principle of Fe-N-C electrocatalysts: how to optimize multimodal porous structures?, *J. Am. Chem. Soc.*, 2019, **141**(5), 2035–2045.
30 M. Qiao, Y. Wang, Q. Wang, *et al.*, Hierarchically ordered porous carbon with atomically dispersed FeN4 for ultraefficient oxygen reduction reaction in proton-exchange membrane fuel cells, *Angew. Chem., Int. Ed.*, 2020, **59**(7), 2688–2694.
31 L. Wang, W. W. Tian, W. Zhang, *et al.*, Boosting oxygen electrocatalytic performance of Cu atom by engineering the d-band center via secondary heteroatomic phosphorus modulation, *Appl. Catal., B*, 2023, **338**, 123043.
32 J. Wei, J. Lou, W. Hu, *et al.*, Superstructured Carbon with Enhanced Kinetics for Zinc-Air Battery and Self-Powered Overall Water Splitting, *Small*, 2024, 2308956.
33 Q. Ye, M. Li, T. Xiao, *et al.*, Ultra-fine Fe_3C nanoparticles decorated in the Fe-N co-doped carbon networks with hierarchical nanoarchitectonics towards efficient oxygen reduction electrocatalysis, *Int. J. Hydrogen Energy*, 2024, **49**, 1014–1021.
34 X. Wen, C. Yu, B. Yan, *et al.*, Morphological and microstructural engineering of Mn-NC with strengthened Mn-N bond for efficient electrochemical oxygen reduction reaction, *Chem. Eng. J.*, 2023, **475**, 146135.
35 J. Nan, S. Shufeng, Y. Juxiang, *et al.*, Carbon material with high pyridine/graphite nitrogen content: an efficient electrocatalyst for the oxygen reduction reaction, *New J. Chem.*, 2024, **48**(2), 640–645.
36 Z. Ma, Y. Duan, Y. Liu, *et al.*, Synergistic effects of hierarchical porous structures and ultra-high pyridine nitrogen doping enhance the oxygen reduction reaction electrocatalytic performance of metal-free laminated lignin-based carbon, *Int. J. Biol. Macromol.*, 2024, **256**, 128292.
37 Q. Xie, M. Pan, Z. Wang, *et al.*, Enhancing the oxygen reduction activity by constructing nanocluster-scaled Fe_2O_3/Cu interfaces, *Nanoscale*, 2023, **15**(9), 4388–4396.
38 Y. Deng, J. Zheng, B. Liu, *et al.*, Schiff-base polymer derived ultralong FeCo/N-doped carbon nanotubes as bifunctional oxygen electrocatalyst for liquid and flexible all-solid-state rechargeable zinc–air batteries, *Carbon*, 2023, **210**, 118000.
39 Q. P. Ngo, T. T. Nguyen, M. Singh, *et al.*, Vanadium tunning amorphous iron phosphate encapsulated iron phosphide on phosphorous-doped graphene promoted oxygen reactions for flexible zinc air batteries, *Appl. Catal., B*, 2023, **331**, 122674.
40 Y. Chen, Y. Wu, L. Li, *et al.*, Hierarchical wood cells impose well-textured carbon nanotubes with cobalt single atoms: Bioinspired construction and application in zinc-air battery, *Chem. Eng. J.*, 2023, **475**, 145993.
41 X. Zhao, Y. Sun, J. Wang, *et al.*, Regulating d-Orbital Hybridization of Subgroup-IVB Single Atoms for Efficient Oxygen Reduction Reaction, *Adv. Mater.*, 2024, 2312117.
42 Z. Li, S. Ji, H. Liu, *et al.*, Constructing Asymmetrical Coordination Microenvironment with Phosphorus-Incorporated Nitrogen-Doped Carbon to Boost Bifunctional Oxygen Electrocatalytic Activity, *Adv. Funct. Mater.*, 2024, **34**(18), 2314444.
43 F. Qiang, J. Feng, H. Wang, *et al.*, Oxygen engineering enables N-doped porous carbon nanofibers as oxygen reduction/evolution reaction electrocatalysts for flexible zinc-air batteries, *ACS Catal.*, 2022, **12**(7), 4002–4015.
44 L. Yang, Y. Zhu, X. Yao, *et al.*, Surface-optimized carbon nanocages with tailorable atomic Fe-N4 sites to boost oxygen reduction in long stable zinc-air battery, *Energy Storage Mater.*, 2023, **63**, 102972.

